nature biotechnology

Multiplexed and scalable super-resolution imaging of three-dimensional protein localization in size-adjustable tissues

Taeyun Ku[1,2,9], Justin Swaney[3,9], Jeong-Yoon Park[1,2,4,9], Alexandre Albanese[1], Evan Murray[1,5], Jae Hun Cho[3], Young-Gyun Park[1,2], Vamsi Mangena[6], Jiapei Chen[7] & Kwanghun Chung[1–3,5,8]

The biology of multicellular organisms is coordinated across multiple size scales, from the subnanoscale of molecules to the macroscale, tissue-wide interconnectivity of cell populations. Here we introduce a method for super-resolution imaging of the multiscale organization of intact tissues. The method, called magnified analysis of the proteome (MAP), linearly expands entire organs fourfold while preserving their overall architecture and three-dimensional proteome organization. MAP is based on the observation that preventing crosslinking within and between endogenous proteins during hydrogel-tissue hybridization allows for natural expansion upon protein denaturation and dissociation. The expanded tissue preserves its protein content, its fine subcellular details, and its organ-scale intercellular connectivity. We use off-the-shelf antibodies for multiple rounds of immunolabeling and imaging of a tissue's magnified proteome, and our experiments demonstrate a success rate of 82% (100/122 antibodies tested). We show that specimen size can be reversibly modulated to image both inter-regional connections and fine synaptic architectures in the mouse brain.

Biological systems such as the mammalian brain consist of thousands of distinct cell types forming highly interconnected functional networks[1–5]. Understanding how these diverse cells interact to generate system-level responses is essential for many fields of biology. Deciphering these complex interactions requires tools that can simultaneously characterize the molecular identity and fine subcellular architectures of individual cells as well as their system-level connectivity, because these properties together determine many cell functions. To date, technologies provide only a subset of the required multilevel information.

Proteomic imaging techniques can potentially provide multilevel information in both animals and human samples[6–10]. The proteome is an ideal substrate for the integrated analysis of functional components owing to proteins' unmatched diversity, functional roles, and distinct subcellular localization at single-molecule precision. The existing large antibody libraries (close to 100,000 antibodies), once rigorously validated, could enable the detection of more than 70% of the human proteome and corresponding cellular architectures[10].

For example, multiplexed proteomic imaging techniques (e.g., array tomography and SWITCH) can provide molecular details for individual cells and may allow reconstruction of their surrounding tissue environment[11–13]. Emerging intact tissue clearing approaches preserve proteins and the continuity of neural fibers, which may enable reconstruction of immunolabeled neural architectures[14,15]. Super-resolution imaging of immunolabeled thin tissue sections has been successfully used to characterize minute subcellular structures (e.g., synapses)[16–19]. In addition to conventional super-resolution approaches, Chen *et al.*[20] have recently demonstrated that protease digestion of a hydrogel-tissue hybrid homogenizes its mechanical characteristics and allows approximately fourfold linear expansion of the hybrid. Using this approach, termed expansion microscopy (ExM), they demonstrated super-resolution imaging of thin tissue sections with custom-made antibody probes and diffraction-limited microscopes[20].

Despite the success of these new technologies, integrated reconstruction of the fine subcellular architectures, molecular details, and intercellular connectivity of diverse cell types in large-scale biological systems remains an unmet goal in biology. For instance, the protease digestion step in ExM causes a loss of proteins, which limits the number of protein structures that can be imaged in the same sample. In addition, intercellular connectivity is largely lost in ExM as it requires tissue sectioning to allow immunolabeling of an unprocessed tissue with limited permeability. By contrast, emerging whole-tissue clearing methods preserve neural connectivity and endogenous proteins, but accurate reconstruction of neural architectures remains challenging owing to the low resolution of diffraction-limited microscopy.

[1]Institute for Medical Engineering and Science, Massachusetts Institute of Technology (MIT), Cambridge, Massachusetts, USA. [2]Picower Institute for Learning and Memory, MIT, Cambridge, Massachusetts, USA. [3]Department of Chemical Engineering, MIT, Cambridge, Massachusetts, USA. [4]Department of Neurosurgery, Gangnam Severance Hospital, Spine and Spinal Cord Institute, Yonsei University College of Medicine, Seoul, Republic of Korea. [5]Department of Brain and Cognitive Sciences, MIT, Cambridge, Massachusetts, USA. [6]Harvard-MIT Division of Health Sciences and Technology, MIT, Cambridge, Massachusetts, USA. [7]Department of Biological Engineering, MIT, Cambridge, Massachusetts, USA. [8]Broad Institute of Harvard University and MIT, Cambridge, Massachusetts, USA. [9]These authors contributed equally to this work. Correspondence should be addressed to K.C. (khchung@mit.edu).

Here we present MAP, a method that enables multiscale proteomic imaging of intact biological systems for combined extraction of the molecular identity, subcellular architectures, and intercellular connectivity of diverse cell types within a single tissue. MAP preserves both the three-dimensional (3D) proteome content and organization and the organ-wide cellular connectivity within an intact tissue-hydrogel hybrid, while rendering it reversibly size-adjustable up to four- to fivefold for multiresolution imaging.

RESULTS

Organ-scale tissue expansion without loss of proteins

The key to MAP is to prevent intra- and interprotein crosslinking during the hydrogel-tissue hybridization step[21], and then to dissociate and denature proteins to allow natural expansion of the hybrid (**Fig. 1a**). We hypothesized that a high concentration of acrylamide monomers might effectively prevent protein crosslinking by quenching reactive methylols formed by the protein-formaldehyde reaction. If the acrylamide monomer concentration is low, the reactive
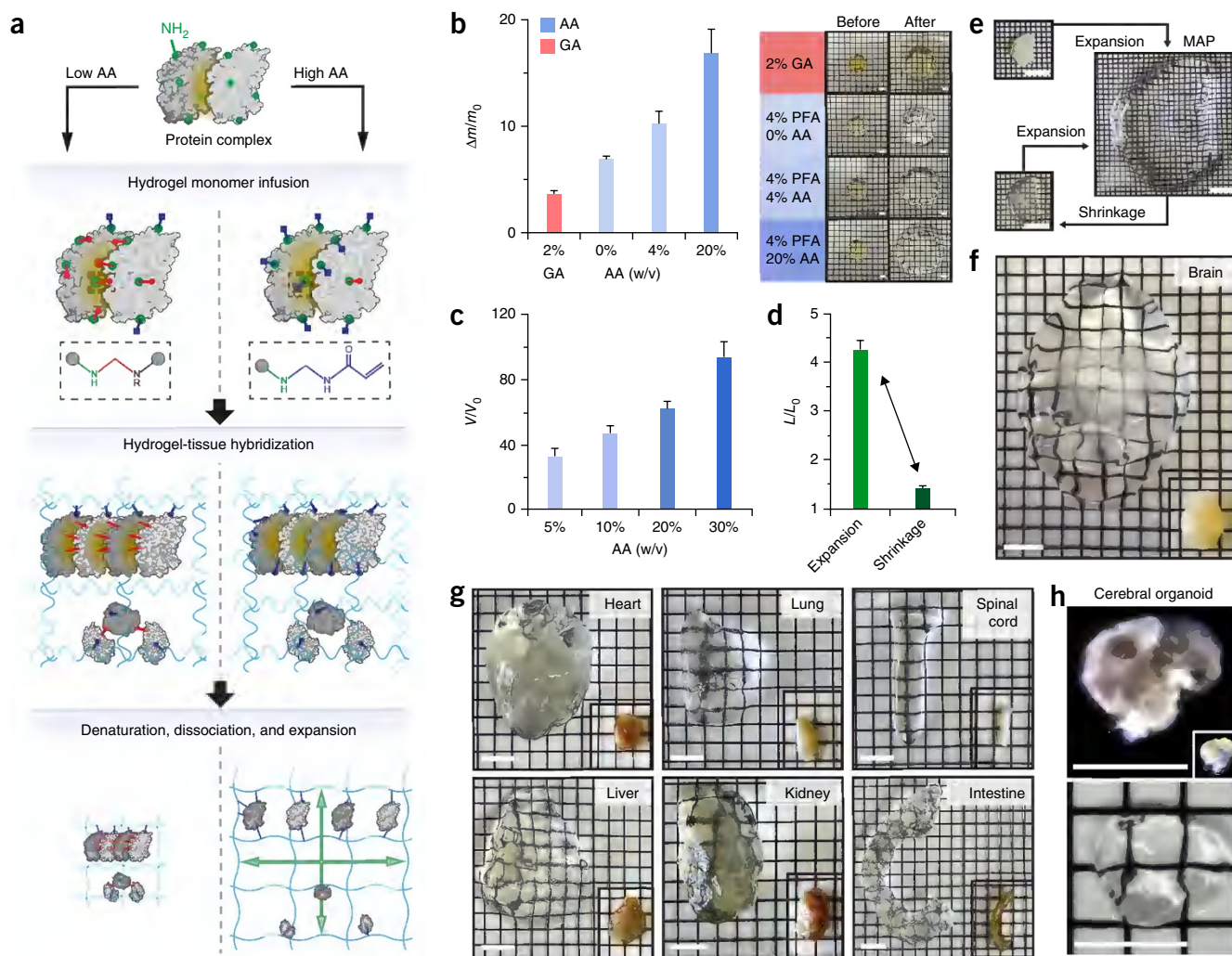

Figure 1 Magnified and accessible 3D proteome library of whole intact organs. (**a**) Comparison of hydrogel-tissue hybridization chemistry, subsequent protein denaturation, and hybrid expansion between low (left column) and high (right column) concentrations of acrylamide (AA; blue) infusion. High-concentration AA prevents intra- and interprotein crosslinking during the hydrogel-tissue hybridization step by quenching reactive methylols formed from amine residues (green) reacting with formaldehyde (red). Dissociation and denaturation of non-crosslinked protein complexes allows natural expansion of the hybrid. In low-concentration AA (left column), the reactive methylols react with available amine or amide groups within the same protein or adjacent proteins and form methylene bridges (red line). Such intra- and interprotein crosslinking prevents complete denaturation and dissociation of the proteins, and thereby limits subsequent tissue expansion. (**b**) Expansion after denaturation of BSA tissue phantom post-fixed in several AA concentrations. Representative images of tissue phantoms before and after expansion are shown. One-way ANOVA was performed (***$P < 0.001$). Error bars show s.d. ($n = 3$). Scale bars, 5 mm. (**c**) Expansion of 1-mm-thick coronal mouse brain slices perfused with several AA concentrations. One-way ANOVA was performed ($P < 0.001$). V_0, volume before expansion; V, volume after expansion. Error bars show mean ± s.d. ($n = 6$). (**d**) Average diameter of 1-mm-thick slices relative to the initial diameter after expansion and subsequent shrinkage. Slices were allowed 24 h for both expansion and shrinkage ($n = 6$). L_0, mean length of original brain; L, mean length after expansion and shrinkage. (**e**) Representative photos showing expansion and shrinkage of a 1-mm-thick coronal block. Starting from the top left, the original brain section, the expanded state, and the shrunken state are shown. (**f**,**g**) MAP applied to a whole mouse brain and other organs. The entire process from perfusion to full expansion took 7 d. Compared with the original organ size (pictures at right bottom corner), the final expansion of the brain showed a more than fourfold increase in length. (**h**) MAP applied to cerebral organoid. Top, darkfield images; bottom, brightfield image. Scale bars (**e**–**h**), 10 mm.

Figure 2 Comparison of multiscale architectures before and after MAP processing. (**a**) HeLa cells stained for alpha-tubulin and imaged before and after MAP processing. (**b**) Fine tubulin structures imaged before and after expansion, respectively. (**c**) Intensity profiles along the paths indicated in **b** based on the pre-expansion size. (**d**) Root-mean-squared measurement error (RMSE) of tubulin images before and after MAP (black line, mean; filled area, s.d.; *n* = 4 samples). (**e**) Morphological image processing of gel-embedded HeLa cells before and after MAP processing. TOTO-1 was used to label nucleic acids. L1 and L2 represent the connecting line segments between two randomly chosen nuclei. (**f**) Local pairwise expansion ratios versus the fraction of the connecting line segment inside of nuclei (black line, overall expansion ratio (3.82); red dashed line, standard linear regression; *m* = 0.04 ± 0.02, *b* = 3.83 ± 0.01). (**g**) RMSE of TOTO-1 images before and after MAP, same as in **d** (*n* = 4 samples). (**h**) 100-μm-thick mouse brain slice showing blood vessels stained with lectin before and after MAP processing. (**i**) RMSE of lectin images same as in **d**. Errors measured after MAP processing (*n* = 6 samples) are compared with errors measured between two rounds of embedding and imaging of the sample before MAP (*n* = 5 samples). (**j**–**l**) 100-μm-thick mouse brain slices stained with anti-GFP antibodies and three other antibodies before and after MAP processing. Magnified 3D-rendered images in middle columns show the same structures imaged with the same microscopic resolution near optical sampling limit. Magnified 2D images showing parvalbumin (PV) ultrastructure in middle panels in **k** were taken from other samples. NF-H, neurofilament heavy unit. (**m**) Intensity plot (left) along the lines in zoom-in single sections (right) of the insets in **j**. The length scale is in terms of distance before MAP. Images were obtained using a 10×, 0.3 NA dry objective (**e**) and a 63×, 1.30 NA glycerol-immersion objective (**a** and **b**) with single-photon (1p) excitation by 488, 568, and 594 nm, and a 20×, 0.95 NA water-immersion objective (**h** and **j**–**m**) at the same resolution below optical sampling limit with either 1p excitation by 488 and 594 nm or 2p excitation by 780 nm. Scale bars, 1 mm (white; **e** and **h**), 100 μm (gray; inset in **e**, and **j**–**l**), 10 μm (yellow; **a**, and insets in **j**–**l**), and 1 μm (magenta; **b** and **m**).
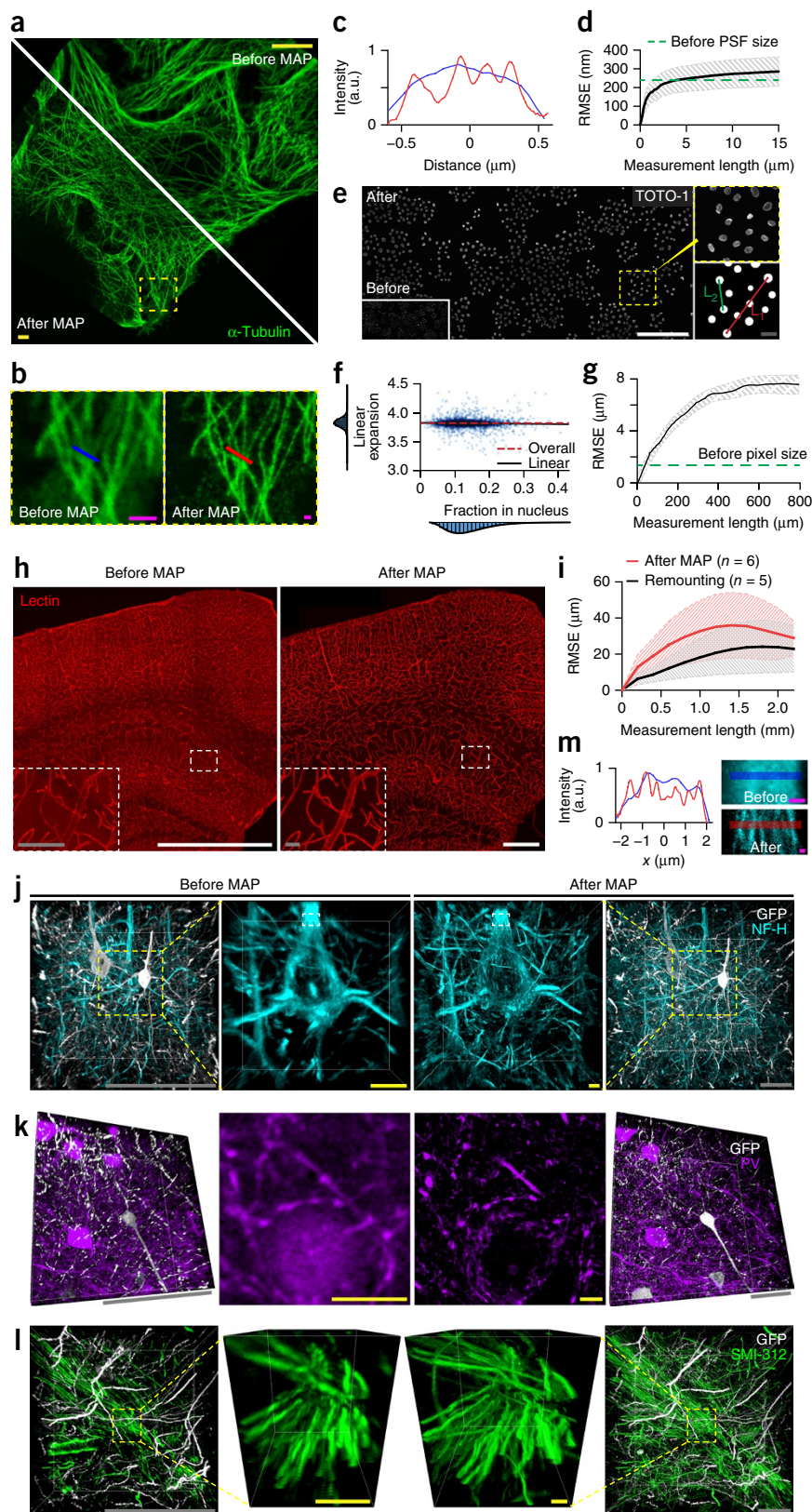
methylols would react with amide groups within the same protein or adjacent proteins to form methylene bridges (**Fig. 1a**, left column)[22]. Such intra- and interprotein crosslinking would prevent dissociation of protein complexes and limit subsequent tissue expansion[23]. With increased acrylamide concentration (**Fig. 1a**, right column), methylols might preferentially react with excess acrylamide monomers, effectively reducing interprotein crosslinking while maximally tethering individual proteins to an expandable hydrogel mesh. Dissociation and denaturation of protein complexes with heat and anionic surfactant then facilitates natural expansion of the hydrogel-tissue hybrid while preserving overall spatial organization of the proteome.

To test our hypothesis, we first measured the effect of acrylamide concentration on tissue expansion. We prepared albumin-containing

Figure 3 Super-resolution imaging showing the 3D proteome library and subcellular details of MAP-processed intact tissue. (**a**) A total of 122 antibodies were tested on MAP-processed mouse brain sections and PFA-fixed control tissues (**Supplementary Table 1**). One hundred of 122 antibodies were compatible with MAP, and 43 of 51 target molecules were successfully labeled. (**b**) Representative images showing morphological details of parvalbumin (PV)-, calbindin (CB)-, and calretinin (CR)-positive cortical neurons. (**c**,**d**) 3D rendering of fine cytoskeletal structures visualized by neurofilament protein staining: NF-H in a cortical neuron (**c**), and SMI-312, a pan-axonal marker, and tyrosine hydroxylase (TH) in a subcortical neuron (**d**). (**e**) Structural relationship between astrocytes and capillaries visualized with glial fibrillary acidic protein (GFAP), lectin, and histone H3 in a subcortical region. (**f**) 3D rendering of a cortical sample stained with neurofilament medium unit (NF-M) and GABA$_B$ receptor subunit-1 antibodies. The inset shows synaptic neurofilaments co-localized with the gabaergic post-synaptic proteins. (**g**) Maximum intensity projection image showing dendritic spines visualized with a cell-type-specific marker, CB. (**h**) Synaptic structure resolved with a pre-synaptic marker, bassoon, and a post-synaptic marker, homer1, in a cortical region. Yellow box shows a GFP-positive neuron whose dendrite was imaged. The inset (white box) highlights the elliptical structures of pre- and post-synaptic proteins distributed at a synaptic junction. (**i**) Intensity plot along the axis of the synapse in **h** (rectangular region, expanded) showing the separation between pre- and post-synaptic distribution profiles. The lines represent the Gaussian curve fitting. (**j**,**l**,**m**) Additional synaptic markers successfully visualizing molecular synapses in MAP-processed tissues. (**j**) A glutamatergic pre-synaptic marker (VGluT2) co-localized with bassoon in a cortical

region (inset). (**k**) Comparison of the number of synapses between bassoon and VGluT2 in **j** (*n* = 3 images). A two-tailed paired *t* test was performed (**P* < 0.05). Error bars show mean ± s.e.m. (**l**) The distribution of glutamatergic pre- (VGluT1) and post-synaptic (PSD95) markers in a cortical region. (**m**) 3D rendering showing the distribution of homer1 clusters in a subcortical region. The images in **f**, **j**, and **m** were obtained from samples stained in a second round. The images were obtained with a 25×, 0.95 NA water-immersion objective (**b**), a 40×, 1.25 NA oil-immersion objective (**e**), and a 63×, 1.30 NA glycerol-immersion objective (**c**, **d**, **f**–**h**, **j**, **l**, and **m**) with 1p excitation (488, 568, 594, and 647 nm). Scale bars, 50 µm (white; **b**–**f** and low magnification images in **h** and **l**), 10 µm (gray; inset in **e**, and **h**, **j**, **l**, and **m**), and 1 µm (yellow; insets in **f**, **h**, **j**, **l**, and **m**).
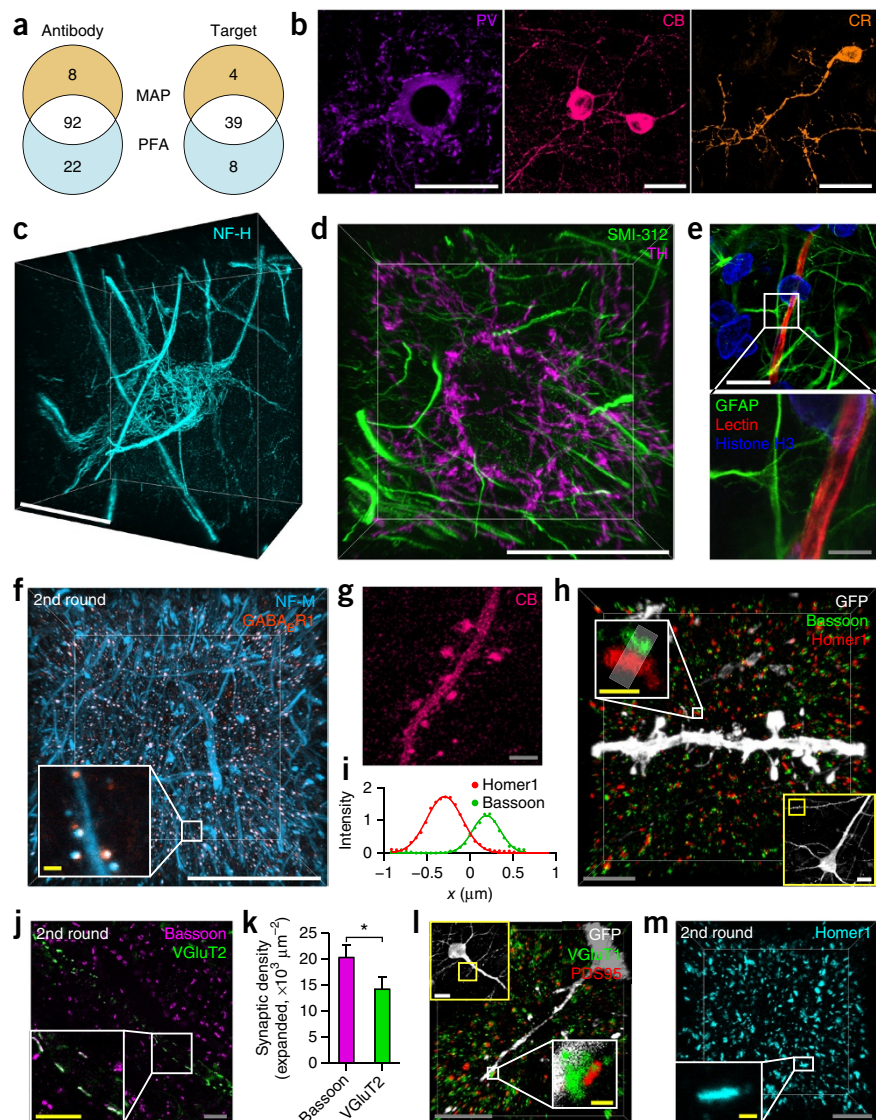
tissue phantoms and post-fixed them in 4% paraformaldehyde (PFA) with different concentrations (0–20%) of acrylamide. We incubated the tissue phantoms in detergent solution at 95 °C for 1 h to denature and disrupt protein aggregates. As expected, phantoms fixed in higher concentrations of acrylamide showed higher degrees of expansion in water (**Fig. 1b**). We observed a similar trend in mouse brain tissues that were perfused with different concentrations of acrylamide, polymerized, denatured, and expanded (**Fig. 1c**). Thus, we used high concentrations of acrylamide in order to maximize expansion during MAP in all subsequent experiments.

Using this approach, we achieved a fourfold linear expansion of a whole mouse brain within 7 d without protease treatment (**Fig. 1f**). Tissue expansion was reversible and tunable using buffers with different salt concentrations and osmolarities (**Fig. 1d,e**). This method

is applicable to other organs including heart, lung, spinal cord, liver, intestine, and kidney, and also cerebral organoids (**Fig. 1g,h** and **Supplementary Fig. 1**).

Preservation of multiscale architectures

We next asked whether MAP retains multiscale structural information and enables super-resolution imaging with diffraction-limited microscopes. To estimate the amount of distortion incurred from expansion, we imaged gel-embedded cultured cells before and after MAP processing (**Fig. 2a**). At the subcellular scale, MAP expansion improved visualization of microtubules and allowed imaging of single tubular structures (**Fig. 2b,c**). The estimated distortion error (root-mean-square error, RMSE) was less than 3% of measured length at both the subcellular scale (**Fig. 2d**) and the multicellular scale (**Fig. 2g**).

Figure 4 Multiplexed staining of MAP-processed tissue. Repeated staining and destaining of a MAP-processed tissue. A 100-μm-thick mouse brain slice including an anterior hippocampal region was used. The tissue in a PBS solution with 0.1% Triton X-100 was imaged. Images are displayed as maximum intensity projection of a 64-μm thickness. Maximum intensity projection images are displayed. Host species of primary antibodies are shown in the parentheses. Break lines indicate destaining. GFP was stained and imaged at 635-nm excitation channel to show consistent labeling of the same antigen. 488- and 559-nm channels were used to show multiplexed labeling of diverse antigens and complete elution of imaged antibodies used in previous rounds. The same imaging and post-processing conditions were used for 635-nm channel images throughout the first and second rounds. MBP, myelin basic protein; TUJ1, neuron-specific class III beta-tubulin. Scale bars, 200 μm.

The degree of gel expansion was not a function of cell density, as indicated by the consistent local expansion within differently populated cell clusters (**Fig. 2e,f**).
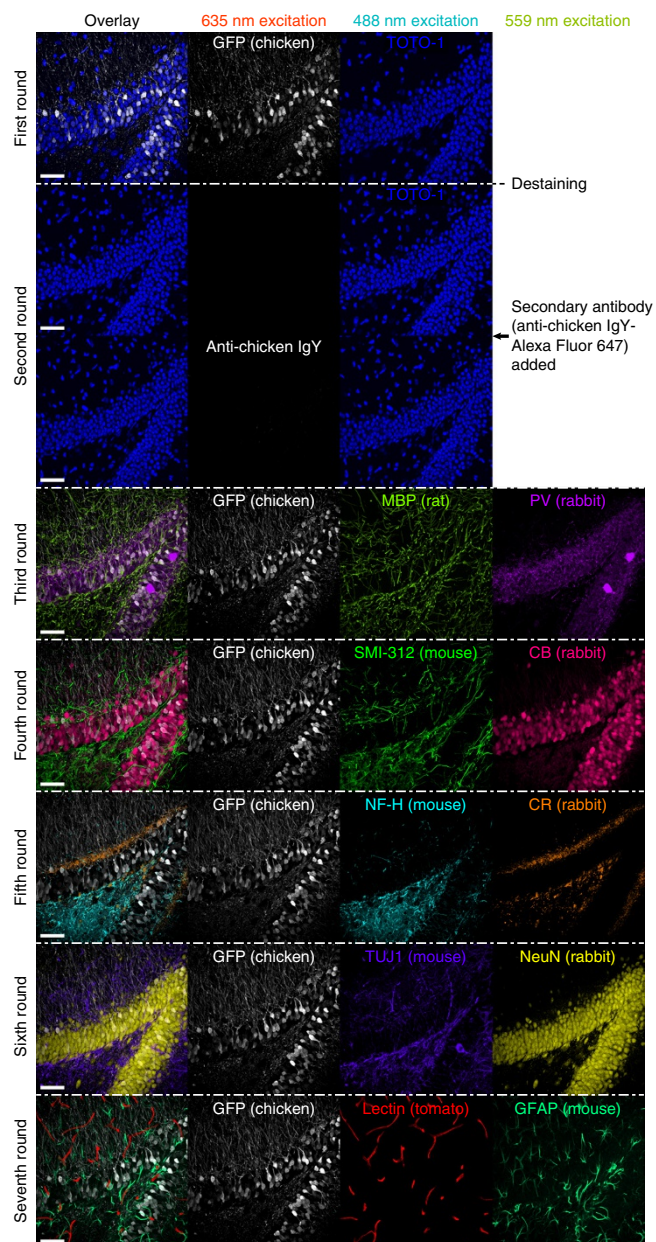
To test whether MAP preserves multiscale tissue architectures, we imaged a 100-μm-thick mouse brain block labeled with lectin before and after MAP (**Fig. 2h**). The distortion analysis showed less than 4% error (**Fig. 2i**), which was at most a twofold increase, compared to the inevitable distortion from sample mounting for imaging (**Fig. 2i**, remounting). Both the intra-vascular space with low protein concentration and the extra-vascular space with high protein concentration showed similar degrees of expansion (**Fig. 2h**, insets), suggesting that the effect of protein concentration and cell density on gel expansion is minimal. Diffraction-limited microscopy revealed fine 3D details of immunolabeled cells such as cytoskeletal filament structures (**Fig. 2j,k,m**) and better-resolved axonal fibers (**Fig. 2l**) after the MAP process. These results together indicate that MAP preserved multiscale structural information of biological samples and enabled super-resolution imaging with diffraction-limited microscopes, achieving ~60-nm lateral resolution.

Labeling proteome with conventional antibodies

We next asked if MAP preserves the 3D proteome composition and organization, and enables super-resolution imaging of fine subcellular architectures using commercially available antibodies. Antibody targets were selected from a wide range of antigens including membrane proteins, cytoplasmic proteins, nuclear proteins, neurofilament proteins, and synaptic proteins to survey the overall proteomic landscape (**Fig. 3** and **Supplementary Table 1**). To validate the antibodies, we tested whether antibody staining of MAP-processed tissues shows comparable structures to PFA-fixed tissues, and antibodies from different host species targeting the same protein, if available, provide concordant images (**Supplementary Figs. 2** and **3**). We found that 100 of 122 antibodies were compatible with MAP-processed samples, and 43 of 51 target molecules were successfully visualized (**Fig. 3**, **Supplementary Table 1**, and **Supplementary Figs. 2** and **3**). This high success rate indicates that loss of epitopes by protein denaturation was minimal. Moreover, some antibodies (e.g., calbindin and calretinin) showed negative staining when different antibodies targeting the same endogenous protein showed strong signal (**Fig. 3b** and **Supplementary Table 1**). This result demonstrates that MAP preserves the tissue proteome with minimal loss of specific epitopes and that the library can be effectively probed using off-the-shelf antibodies without any modification.

Super-resolution imaging of 3D subcellular architectures

Preservation of both nanoscopic structures and the proteome in MAP enables super-resolution imaging of a broad range of fine subcellular architectures. Antibodies targeting filament proteins successfully visualized details of the cytoskeletal networks of various cell types (**Fig. 3c–e** and **Supplementary Videos 1–4**). No apparent filament fragmentations were observed in the magnified tissues. Labeling of glial fibrillary acidic protein (GFAP) enabled visualization the fine foot-process structures surrounding blood vessels (**Fig. 3e** and **Supplementary Video 3**)[24,25]. Neurofilament medium subunit (NF-M) enabled visualization of both processes and synapses[26], a subset of which co-localized with the postsynaptic marker, GABA$_B$R1 (the C-terminal domain of the GABA$_B$ receptor subunit-1) (**Fig. 3f** and **Supplementary Video 4**). Labeling of calcium-binding proteins (parvalbumin, calbindin, and calbindin) robustly enabled visualization of morphological details of positive cells (**Fig. 3b**). A small subset of calbindin-positive fibers showed expression of calbindin in their dendritic spines (**Fig. 3g**). Many synaptic protein markers were compatible with MAP (**Fig. 3f,h,j,l,m** and **Supplementary Table 1**). Staining of synaptic proteins clearly visualized distinct and

Figure 5 Intercellular connectivity and its reconstruction at single-fiber resolution in MAP-processed tissue. (**a–g**) Connectivity and morphology of cells are preserved in the MAP-processed tissue. (**a**) A 500-µm-thick slice of a mouse brain hemisphere stained with anti-GFP antibody and imaged after expansion and shrinkage. (**b**) The entire neuronal territory and axon fiber of a cortical pyramidal neuron included within the yellow-boxed region in the left panel. The volume was 3D reconstructed with background removal. (**c–e**) Images of the same neuron in **b** obtained with a 10×, 0.3 NA objective (**c,d**) and a 10×, 0.6 NA objective (**e**), showing its morphological details before MAP, after MAP expansion, and after MAP shrinkage. (**f,g**) Fine subcellular structures preserved and resolved in the expansion states: dendritic network (**f**) and dendritic spines (**g**). (**h–l**) Neuronal fibers and cell body (asterisks) morphology visualized using various markers (CR, SMI-32, NF-H, SMI-312, and TH) in different cortical (**i–k**) and subcortical (**l**) regions of a 1-mm-thick hemisphere slice (**h**). The inset in **i** shows the isolated neuronal cell body and its axon with background removal. (**m**) Long-range tracing (white line, longer than 3 mm) of an inter-regional TH neurofilament within the magenta box in **h**. (**n**) Subvolume within a square region in **h** (green box) containing dense SMI-312–positive fibers. The red line shows a tracing result across the volume. (**o**) One of the densest subregions in the left inset in **n** visualizing all individual fibers resolved and traced. (**p**) A dense region in the right inset in **n** showing closely crossing fibers. Depth-color coding of the fibers clearly shows good separation along the z-axis. (**q**) The intensities of the two fibers closely located in a similar plane in **p** are plotted and fitted to Gaussian curves to show their clear separation. (**r,s**) Comparison of manual tracing results of a 100-µm-thick hippocampal sample stained with SMI-312 before (**r**) and after (**s**) MAP processing. Apparently detectable fibers were traced by two individuals. Discordant traces are selectively displayed for before MAP image (**r**),

and the same traces, which resulted in concordant tracing after expansion, are shown for after MAP image (**s**). (**t,u**) Comparison of discordance ratios between manual tracing results before and after MAP processing. Two markers (SMI-312 and NF-H) were used with four regions of interest for each marker. Two-tailed paired t tests were performed (**P < 0.01, *P < 0.05). Error bars show mean ± s.e.m. Images were obtained using a 10×, 0.6 NA CLARITY-optimized objective (**a–c, e**), a 10×, 0.3 NA water-immersion objective (**d**), a 20×, 0.95 NA water-immersion objective (**m**), a 63×, 1.30 NA glycerol-immersion objective (**l** and **n–p**), and a 25×, 0.95 NA water-immersion objective (**f, g, i–k, r**, and **s**) with 1p excitation by 488, 568, and 594 nm. Scale bars, 1 mm (gray; **a**), 200 µm (white; **b–f, i–k, m, n**), and 10 µm (yellow; **g, l, o**, and **p, r**, and **s**).
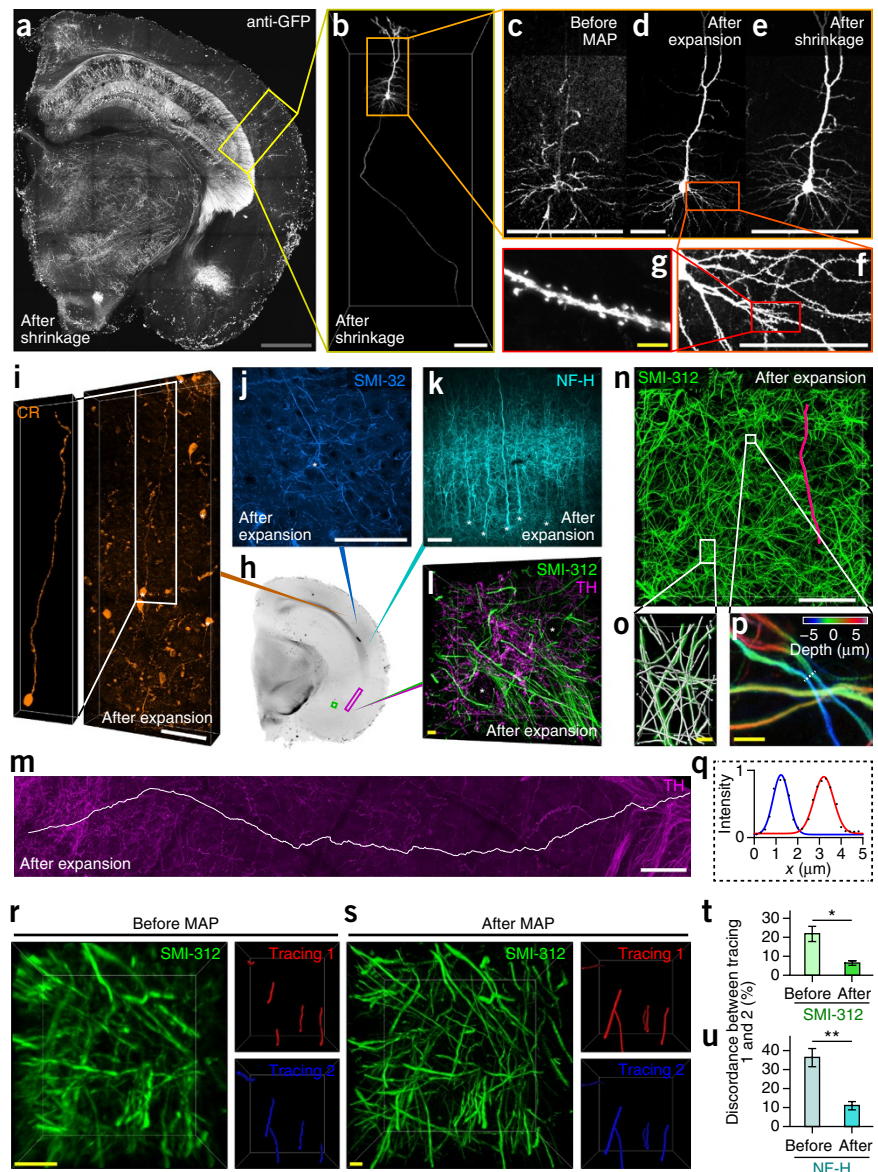
well-separated elliptical disk-shaped clusters of pre- and post-synaptic proteins (**Fig. 3h,l,m** and **Supplementary Video 5**), enabling their quantitative analysis (**Fig. 3k**).

Highly multiplexed immunolabeling

Another potential advantage of the MAP technology is that it enables highly multiplexed labeling and imaging of the magnified 3D proteome within a single tissue. We successfully performed seven rounds of immunostaining of a MAP-processed 100-µm-thick mouse brain tissue with no obvious signs of tissue damage (**Fig. 4**). Outstanding mechanical stability of the MAP-processed sample enabled repeated manual handling of the tissue with tools that are widely used in biology laboratories. The images after destaining of the imaged anti-GFP

antibody (first round) and after solely adding secondary antibodies targeting the eluted anti-GFP antibody (second round) showed little signal, suggesting that the destaining process effectively eliminates antibodies. For the following five rounds of labeling, we continued to use anti-GFP as a landmark in addition to two other antibodies for each round. The consistent GFP signals show that the same antigen can be repeatedly labeled without loss of antigenicity. Successful visualization of ten other targets demonstrated that MAP facilitated exploration of diverse proteins, structures, and cell types within a single tissue.

MAPing neural projections

We next explored the potential utility of MAP for mapping inter-areal neural connectivity. If MAP could preserve continuity

Figure 6 Immunolabeling and imaging of thick MAP-processed tissues. (**a**–**e**) Passive staining of a 1-mm-thick (5 mm after expansion) dorsolateral mouse brain slice with anti-GFP antibodies. (**a**) The tissue was incubated for 3 d with primary antibody and 3 d with secondary antibody, and expanded in DI water. (**f**–**j**) Stochastic electrotransport[28] staining of a 2-mm-thick (8 mm after expansion) mouse hemisphere slice with anti-GFP antibodies. (**f**) The tissue was stained for 1 d with both primary and secondary antibodies. (**b**,**g**) Lateral (top panels) and top (bottom panels) views of the sample. White boxes indicate the regions of interest for z-stack images. The cortical (**b**) and hippocampal (**g**) regions were chosen at least 2.5- and 4-mm far from the lateral tissue boundary, respectively, to exclude the chance of dominant staining by lateral diffusion at a middle section. (**c**,**h**) Laser power used along depth to obtain a z-stack image. (**d**,**i**) Longitudinal tile-scan images along z-axis with 1p excitation and a 10×, 0.6 NA, 8-mm WD objective. (**e**,**j**) Sectional images at different depths either with a 10×, 0.6 NA, 8-mm WD (magenta) or a 20×, 0.95 NA, 2-mm WD (blue) objectives. The same image acquisition parameters were used for sectional images with each objective. Insets in **e** are zoom-in images showing dendritic spines. Scale bars, 5 mm (gray; **b** and **g**), 500 µm (white; **d** and **i**), 100 µm (yellow; **e** and **j**), and 10 µm (blue; insets in **e**).
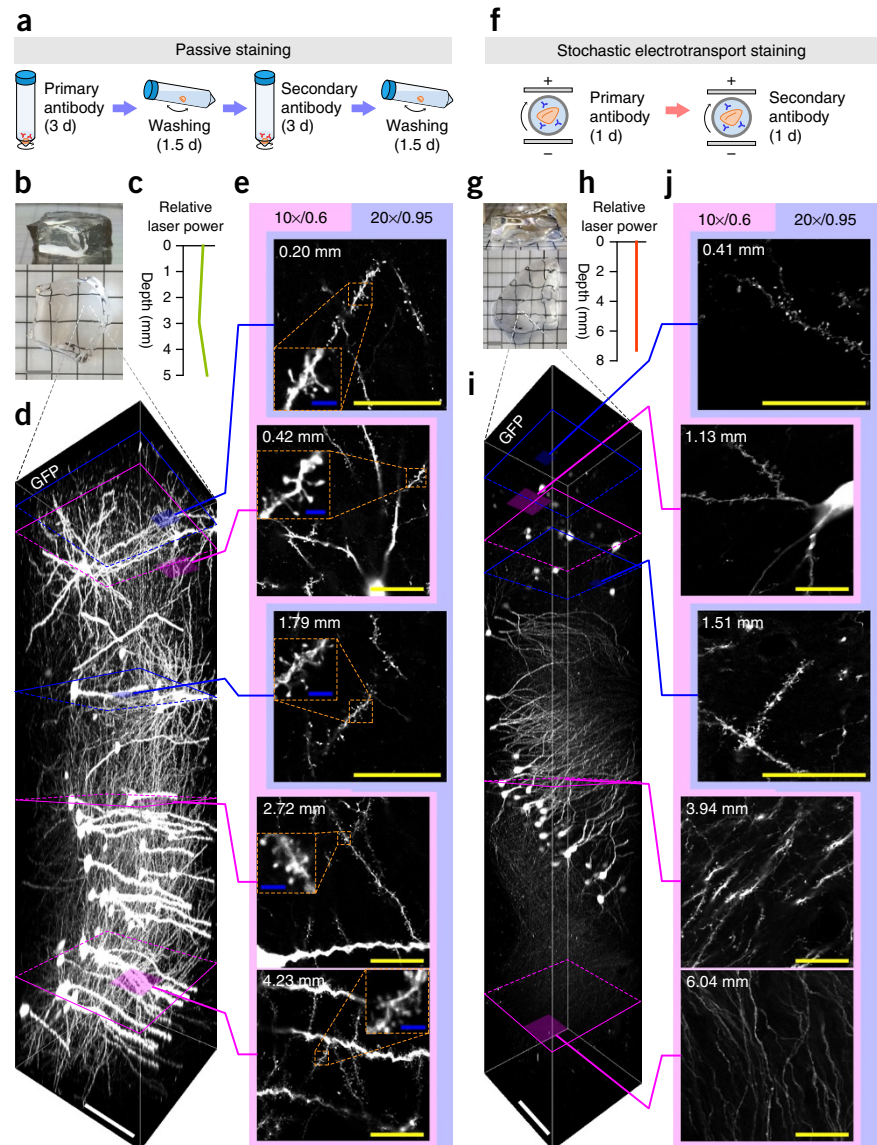
of neural fibers within magnified, intact brain tissue along with its 3D proteome, highly specific antibodies would enable visualization of a subset of neural projections connecting different brain regions. The sparse labeling and enhanced spatial resolution offered by MAP may allow more accurate reconstruction of the labeled projections. In addition, highly multiplexed proteomic imaging may enable reconstruction of many different cell types with integrated molecular and fine morphological details in a single tissue.

To explore this possibility, we first asked if the continuity of neural processes is preserved within a magnified sample. We expanded a 0.5-mm-thick Thy1-eGFP mouse brain coronal block and then imaged GFP-labeled neurons and their projections[27]. MAP preserved the continuity of the GFP-expressing projections spanning a large tissue volume (**Fig. 5a**–**f**) as well as their fine morphological details (e.g., dendritic spines) (**Fig. 5g**). Immunolabeling of various cytoplasmic proteins including neurofilament proteins (e.g., NF-H and SMI-32), calcium-binding proteins, and metabolic enzymes (e.g., tyrosine hydroxylase) confirmed that MAP preserved the continuity of neural fibers of various cell types (**Fig. 5h**–**n** and **Supplementary Videos 6**–**8**). The preserved continuity enabled detection of single fibers selected in the immunostained tissue volumes (**Fig. 5m**–**q** and **Supplementary Videos 7** and **8**).

To test if MAP enables more accurate tracing of densely packed fibers, we imaged neurofilament-stained samples before and after MAP processing using a high numerical aperture (NA; 0.95) water-immersion objective. Two individuals not involved in image

acquisition traced fibers within the sample volume (**Fig. 5r,s**). When we compared the concordance between the two tracing results, the discordant rate was significantly lower after MAP (**Fig. 5t,u**; SMI-312, $n = 4$, $P = 0.020$; NF-H, $n = 4$, $P = 0.010$), even though MAP enabled the tracers to detect more fibers (total numbers of traced fibers were 160 before MAP and 214 after MAP). This result demonstrates that MAP indeed enabled more accurate reconstruction of immunolabeled neural fibers.

Immunolabeling and imaging of mm-thick tissues

Reconstruction of individual neurons requires labeling and imaging of thick brain tissues because nerve fibers can extend across a large volume. To test whether MAP is applicable to large-scale brain tissues, we expanded a 1-mm-thick mouse brain block (5-mm thick after expansion, **Fig. 6b**) and passively stained it with anti-GFP antibody (**Fig. 6a**). We then imaged the sample using both a high NA (0.95), short working distance (WD) (2 mm) water-immersion objective and a low NA (0.6), long WD (8 mm) CLARITY objective. Both objectives showed fine dendritic spines of GFP-expressing neurons throughout the entire volume (**Fig. 6e**). Imaging of the sample did not require

depth-dependent modulation of the laser power, indicating that staining was uniform and that signal attenuation by light scattering was negligible (**Fig. 6c,d**). MAP is also compatible with stochastic electrotransport[28], a method that enables rapid tissue labeling. Using stochastic electrotransport, we were able to label an 8-mm-thick expanded tissue uniformly within only 2 d (**Fig. 6f–j**). The sample was highly transparent. We were able to image the 8-mm-thick sample successfully with the same laser power up to the working distance of the objective (**Fig. 6h**).

DISCUSSION

As a step toward organ-scale reconstruction of diverse cell types and their surrounding environment and to advance the study of complex system-level interactions, we developed a simple and scalable method that enables preservation, reversible expansion, and imaging of the 3D proteome organization within an intact tissue. We discovered that the protein content of a whole organ can be preserved and magnified by preventing intra- and interprotein crosslinking, then denaturing and dissociating the protein complexes to allow natural expansion of hydrogel-tissue hybrids. The expanded hybrids secure both fine subcellular architectures and organ-scale cellular connectivity. These multiscale properties can be directly imaged by using off-the-shelf antibodies to label the structures' constituent proteins. The high success rate that we achieved with commercial antibodies might be because synthetic peptides or denatured protein fragments are commonly used for conventional antibody production[29]. An existing large antibody library, once validated, can be used without any modification. This technique is easy to implement, and it does not require any special equipment or chemicals.

MAP enables repeated interrogation of the same expanded specimen. This is possible because the preserved epitopes, which have already reached complete denaturation by harsh treatment (95 °C, 200 mM sodium dodecyl sulfate (SDS)) for expansion, do not undergo any substantial modification during the milder antibody elution step (70 °C, 200 mM SDS). We performed seven rounds of staining of the same tissue without any signs of tissue damage. However, the practical limit of this approach must be carefully examined.

MAP has the potential to enable scalable super-resolution imaging of large-scale samples. Unlike other methods, thick tissues can be labeled on a practical time scale because antibody-labeling occurs after complete lipid removal and tissue permeabilization. The great transparency of the MAP-processed samples allows high-resolution imaging of the physically expanded tissue with minimal loss of resolution. Currently, 1.0 NA, 2.5-mm WD water-immersion objectives are best suited for MAP. Although the 1.0 NA, 8-mm WD CLARITY objective has the longest WD, it does not provide high-quality images because it is optimized for immersion media with a high refractive index (RI). Further development of high-NA, long-WD water objectives or the development of high-RI immersion media that are compatible with MAP would extend the utility of MAP. Another challenge in the MAP approach is the dilution of fluorescent signals that accompanies physical volumetric expansion. Fourfold linear expansion decreases signal density by 64-fold. Therefore, much higher laser power is required, which in turn causes photobleaching. Future studies will need to explore the compatibility of signal amplification techniques with MAP.

The reversible modulation of physical sample size that is attained with MAP enables multiscale proteomic imaging of a single tissue to capture both system-scale properties and fine local details in a practical way. For example, following sample shrinkage, global projection patterns of labeled neurons may be imaged using high-speed microscopy

techniques and long WD objectives (e.g., 25×, 1.0 NA, 8-mm WD objective, currently available)[30]. After imaging, the same tissue can be expanded for super-resolution imaging of regions of interest. The expanded tissue may need to be sliced before imaging to meet the objective's WD limit. A microscope with a built-in vibrating-blade microtome could also be used for whole-mount imaging to avoid loss of connectivity information[31–33]. This approach may allow us to drastically reduce the imaging time and costs associated with data storage and handling of expanded samples.

The advantages of MAP (**Supplementary Table 2**) may allow combined extraction of rich molecular details, minute subcellular architectures, and cellular connectivity from diverse cell types within a single tissue. Together with its simplicity and broad applicability, MAP may complement existing methods and enable new approaches in the study of complex biological systems.

METHODS

Methods and any associated references are available in the online version of the paper.

Note: Any Supplementary Information and Source Data files are available in the online version of the paper.

1. White, J.G., Southgate, E., Thomson, J.N. & Brenner, S. The structure of the nervous system of the nematode *Caenorhabditis elegans. Philos. Trans. R. Soc. Lond., B* **314**, 1–340 (1986).
2. DeFelipe, J. From the connectome to the synaptome: an epic love story. *Science* **330**, 1198–1201 (2010).
3. Helmstaedter, M. Cellular-resolution connectomics: challenges of dense neural circuit reconstruction. *Nat. Methods* **10**, 501–507 (2013).
4. Craddock, R.C. *et al.* Imaging human connectomes at the macroscale. *Nat. Methods* **10**, 524–539 (2013).
5. Oh, S.W. *et al.* A mesoscale connectome of the mouse brain. *Nature* **508**, 207–214 (2014).
6. Phizicky, E., Bastiaens, P.I., Zhu, H., Snyder, M. & Fields, S. Protein analysis on a proteomic scale. *Nature* **422**, 208–215 (2003).
7. Hanash, S. HUPO initiatives relevant to clinical proteomics. *Mol. Cell. Proteomics* **3**, 298–301 (2004).
8. Agaton, C., Uhlén, M. & Hober, S. Genome-based proteomics. *Electrophoresis* **25**, 1280–1288 (2004).
9. Berglund, L. *et al.* A genecentric Human Protein Atlas for expression profiles based on antibodies. *Mol. Cell. Proteomics* **7**, 2019–2027 (2008).
10. Uhlen, M. *et al.* Towards a knowledge-based human protein atlas. *Nat. Biotechnol.* **28**, 1248–1250 (2010).
11. Micheva, K.D. & Smith, S.J. Array tomography: a new tool for imaging the molecular architecture and ultrastructure of neural circuits. *Neuron* **55**, 25–36 (2007).

12. Kay, K.R. *et al.* Studying synapses in human brain with array tomography and electron microscopy. *Nat. Protoc.* **8**, 1366–1380 (2013).
13. Murray, E. *et al.* Simple, scalable proteomic imaging for high-dimensional profiling of intact systems. *Cell* **163**, 1500–1514 (2015).
14. Dodt, H.-U. *et al.* Ultramicroscopy: three-dimensional visualization of neuronal networks in the whole mouse brain. *Nat. Methods* **4**, 331–336 (2007).
15. Richardson, D.S. & Lichtman, J.W. Clarifying tissue clearing. *Cell* **162**, 246–257 (2015).
16. Rust, M.J., Bates, M. & Zhuang, X. Sub-diffraction-limit imaging by stochastic optical reconstruction microscopy (STORM). *Nat. Methods* **3**, 793–795 (2006).
17. Betzig, E. *et al.* Imaging intracellular fluorescent proteins at nanometer resolution. *Science* **313**, 1642–1645 (2006).
18. Hess, S.T., Girirajan, T.P. & Mason, M.D. Ultra-high resolution imaging by fluorescence photoactivation localization microscopy. *Biophys. J.* **91**, 4258–4272 (2006).
19. Maglione, M. & Sigrist, S.J. Seeing the forest tree by tree: super-resolution light microscopy meets the neurosciences. *Nat. Neurosci.* **16**, 790–797 (2013).
20. Chen, F., Tillberg, P.W. & Boyden, E.S. Optical imaging. Expansion microscopy. *Science* **347**, 543–548 (2015).
21. Chung, K. & Deisseroth, K. CLARITY for mapping the nervous system. *Nat. Methods* **10**, 508–513 (2013).
22. Puchtler, H. & Meloan, S.N. On the chemistry of formaldehyde fixation and its effects on immunohistochemical reactions. *Histochemistry* **82**, 201–204 (1985).
23. Sung, H.-W., Hsu, H.-L., Shih, C.-C. & Lin, D.-S. Cross-linking characteristics of biological tissues fixed with monofunctional or multifunctional epoxy compounds. *Biomaterials* **17**, 1405–1410 (1996).
24. Kosaka, T. & Hama, K. Three-dimensional structure of astrocytes in the rat dentate gyrus. *J. Comp. Neurol.* **249**, 242–260 (1986).
25. Khakh, B.S. & Sofroniew, M.V. Diversity of astrocyte functions and phenotypes in neural circuits. *Nat. Neurosci.* **18**, 942–952 (2015).
26. Yuan, A. *et al.* Neurofilament subunits are integral components of synapses and modulate neurotransmission and behavior *in vivo. Mol. Psychiatry* **20**, 986–994 (2015).
27. Feng, G. *et al.* Imaging neuronal subsets in transgenic mice expressing multiple spectral variants of GFP. *Neuron* **28**, 41–51 (2000).
28. Kim, S.Y. *et al.* Stochastic electrotransport selectively enhances the transport of highly electromobile molecules. *Proc. Natl. Acad. Sci. USA* **112**, E6274–E6283 (2015).
29. Uhlen, M. & Ponten, F. Antibody-based proteomics for human tissue profiling. *Mol. Cell. Proteomics* **4**, 384–393 (2005).
30. Tomer, R., Ye, L., Hsueh, B. & Deisseroth, K. Advanced CLARITY for rapid and high-resolution imaging of intact tissues. *Nat. Protoc.* **9**, 1682–1697 (2014).
31. Ragan, T. *et al.* Serial two-photon tomography for automated *ex vivo* mouse brain imaging. *Nat. Methods* **9**, 255–258 (2012).
32. Economo, M.N. *et al.* A platform for brain-wide imaging and reconstruction of individual neurons. *eLife* **5**, e10566 (2016).
33. Albanese, A. & Chung, K. Whole-brain imaging reaches new heights (and lengths). *eLife* **5**, e13367 (2016).

ONLINE METHODS

BSA hydrogel denaturation and expansion. Stock solutions of 40% BSA, 40% acrylamide (AA), 32% paraformaldehyde (PFA), and 1% VA-044 were made and kept on ice throughout the experiment. A 10-mL solution of 4% BSA, 4% AA, 4% PFA, 0.1% bis-acrylamide (BA), and 0.1% VA-044 was made in phosphate-buffered saline (PBS). The solution was polymerized under vacuum at 37 °C for 2 h, and the resulting albumin-containing tissue phantom was sectioned. Individual tissue phantom sections were washed in excess PBS with shaking for 12 h. After washing, four phantoms were placed in 10 mL of each of the following PBS solutions for 4 h at 37 °C: 2% glutaraldehyde (GA), 4% PFA, 4% AA with 4% PFA, and 20% AA with 4% PFA. Tissue phantoms were washed similarly, massed, photographed, and then incubated in a 200-mM SDS solution with 50 mM sodium sulfite for 1 h at 95 °C. Phantoms were washed again and incubated in deionized (DI) water for 12 h. After expansion, phantoms were massed and photographed.

General MAP protocol. *i. Perfusion and hydrogel embedding.* Thy1-eGFP-M mice (6–8 weeks old, male and female) were housed in a reverse 12-h light/dark cycle with unrestricted access to food and water. All experimental protocols were approved by the MIT Institutional Animal Care and Use Committee and the Division of Comparative Medicine and were in accordance with guidelines from the US National Institutes of Health. After anesthesia, the mice were first washed transcardially with a mixture of 2–5% AA, 0–0.05% BA, 0–0.8% sodium acrylate (SA), and PBS, followed by perfusion with a mixture of 4% PFA, 30% AA, 0.05–0.1% BA, 10% SA, 0.1% VA-044 or V-50, and PBS. The perfusion solution could be slightly turbid. Upper transparent solution was used after centrifugation during 3 min with 1,000*g*. All solution was protected from light and kept on ice before perfusion. Control samples were perfused first with PBS and then with 4% PFA and PBS. The brain and other organs (heart, lung, liver, intestine, kidney, and spinal cord) were harvested and incubated in 20–40 mL of the same fixative solution at 4 °C for 2–3 d and then for 1–3 d at room temperature (RT) with gentle shaking to ensure uniform chemical diffusion and reaction throughout the sample. Following the diffusion and fixation steps, hydrogel-tissue hybridization was performed *in situ* by incubating the tissues using Easy-Gel (LifeCanvas Technologies) with nitrogen gas at 45 °C for 2 h.

ii. Tissue denaturation. Hydrogel-embedded tissues were incubated overnight in a solution of 200 mM SDS, 200 mM NaCl, and 50 mM Tris in DI water (pH titrated to 9.0) at 37 °C with gentle shaking. The samples were then incubated at 70 °C for 0–50 h and 95 °C for 1–24 h depending on their size using EasyClear (LifeCanvas Technologies). Whole organs were incubated for 24–48 h at 70 °C followed by 12–24 h at 95 °C. 1-mm-thick brain slices were incubated for 5 h at 70 °C and then at 95 °C for 1 h.

iii. Expansion. Denatured tissues were incubated in 40–100 mL DI water at RT for 12–48 h with gentle shaking. During DI water incubation, the solution was changed every 3–5 h.

Expansion according to various AA and SA concentrations. After anesthesia, mice were washed transcardially with 4% AA, 0.05% BA, 0.8% SA, 0.1% VA-044, and PBS and then with 4% PFA, 0.05% BA, 0.1% VA-044, one of four AA and SA combinations (5% AA + 0.8% SA, 10% AA + 1.7% SA, 20% AA + 3.3% SA, and 30% AA + 5% SA) in PBS. Tissues were incubated in 20 mL of the same fixative solution at 4 °C for 2 d and 5 h at RT with gentle shaking. After hydrogel-tissue hybridization the samples were incubated in denaturation solution at 70 °C for 5 h and 95 °C for 1 h with gentle shaking. Denatured tissues were incubated in 40 mL DI water at RT for 12 h with gentle shaking. During DI water incubation, the solution was changed every 3–5 h. Fiji (National Institutes of Health) was used to measure the size of the expanded samples[34].

Shrinkage and RI matching. A customized RI matching solution was made by dissolving 50 g diatrizoic acid, 40 g *N*-methyl-D-glucamine, and 55 g iodixanol per 100 mL PBS[28]. The RI was targeted to 1.47. This solution was used for both shrinkage and imaging. Depending on sample size, samples were incubated in 1–10 mL solution at RT for 2–24 h with gentle shaking. The solution was changed every 1–12 h. For imaging tissues before MAP

processing, samples were incubated in 1–10 mL of this solution without PBS at RT with gentle shaking for 2–5 h before imaging.

MAP processing of cerebral organoid. Cerebral organoids were made from stem cells following a previously described protocol[35]. Organoids were initially fixed in 4% PFA for 15 min, incubated in a mixture of 4% PFA, 30% AA, 0.1% BA, 10% SA, 0.1% V-50, and PBS for 24 h at 4 °C, followed by 24 h, at RT. Hydrogel embedding, tissue denaturation, and expansion were processed similarly to "General MAP protocol."

Cultured cell experiment. For tubulin imaging in HeLa cells, 8-mm round glass coverslips were coated in 0.1% gelatin in ultrapure water (Millipore). Coverslips were placed in a 48-well plate and seeded with 50,000 HeLa cells overnight. To obtain comparable images before and after MAP processing, cells were washed, fixed with 3% PFA + 0.1% GA in PBS for 10 min, and switched to a solution of 4% PFA, 30% AA in PBS for 8 h at 37 °C. Cells were then placed in 0.1% sodium borohydride for 7 min at RT then incubated in 100 mM glycine for 10 min at RT. Cells were washed and stained with anti-tubulin (Abcam, ab6160), Alexa Fluor 594-conjugated secondary (Abcam, ab150152) antibodies and TOTO-1 (Thermo Fisher Scientific). Cells were mounted in 2,2′-thiodiethanol (Sigma) and imaged with a 63×, 1.3 NA glycerol-immersion objective with the Leica microscope system. Cells were washed extensively and embedded into a MAP hybrid polymer by addition of 20 µL of Cell-MAP solution (20% AA, 7% SA, 0.1% BA, 0.5% TEMED, 0.5% ammonium persulfate in PBS). Ammonium persulfate was added last from a freshly prepared 5% stock solution. Cell-MAP solution was quickly added to the coverslip and left to polymerize for 4–5 min. Gels were peeled off the coverslip using forceps, washed extensively and denatured for 30 min in denaturation buffer at 95 °C. Cell-MAP gels were washed extensively, restained with anti-tubulin antibody and TOTO-1 and reimaged.

Immunostaining of brain tissue. For typical staining, MAP-processed 100- to 500-µm-thick mouse brain coronal slices were incubated with primary antibodies (typical dilution, 1:100) in PBS with 1% (wt/vol) Triton X-100 (PBST) at 37 °C for 8–16 h, followed by washing at 37 °C for 1–2 h in PBST three times. The tissue was then incubated with secondary antibodies (typical dilution, 1:100) in PBST at 37 °C for 6–16 h, followed by washing at 37 °C for 1–2 h in PBST three times. For antibody validation of a given antibody, 100-µm-thick PFA-fixed control and MAP-processed samples were stained with the same titer of primary and, if necessary, secondary antibodies overnight in PBST. See **Supplementary Table 1** for the list of antibodies used. To destain for multiplexed labeling, samples were incubated in a denaturation solution 6–16 h at 70 °C, and washed with PBST at 37 °C for 1–2 h three times.

Mounting and imaging. Samples were mounted on a slide glass. Blu-Tack adhesive was applied on the Petri dish or the slide glass, and samples were covered with a glass-bottom Willco dish. The space between the bottom material and the Willco dish around the sample was filled with either shrinkage solution or DI water according to the sample immersion medium. Large expanded samples were additionally placed on a 120-mm-diameter Petri dish, and the dish was filled with DI water. Expanded or shrunk samples were stabilized for at least 1 h before imaging. Samples were imaged with either the Olympus FV1200MPE microscope system or the Leica TCS SP8 microscope system. A 10×, 0.6 NA CLARITY-optimized objective (XLPLN10XSVMP; 8.0-mm WD) was used with the Olympus system to obtain wide-field images of shrunk samples and *z*-stack images of large samples. The images of MAP-processed samples were obtained with a 10×, 0.3 NA water-immersion objective, a 20×, 0.95 NA water-immersion objective, and a 40×, 1.25 NA oil-immersion objective with the Olympus system, or a 10×, 0.3 NA water-immersion objective, a 25×, 0.95 NA water-immersion objective, and 63×, 1.30 NA glycerol-immersion objective with the Leica system. Single-photon confocal laser scanning imaging was performed with 405-, 488-, 559-, and 635-nm lasers (Olympus) or a white-light laser (Leica). Mai Tai DeepSee (Spectra-Physics) was used for multi-photon excitation with 780-nm wavelength. The images were visualized and analyzed with Fiji or Imaris (Bitplane).

Large tissue staining. 1- and 2-mm-thick mouse brain coronal slices were prepared by "General MAP protocol," and expanded. A 1-mm-thick slice was chopped to about 3 mm × 3 mm × 1 mm (dimensions before MAP). The sample was stained passively with Alexa Fluor 594-conjugated rabbit anti-GFP antibody (Life Technologies, A21312) for 3 d and Alexa Fluor 594-conjugated donkey anti-rabbit IgG antibody (Abcam, ab150072) for 3 d. 20 μL of antibody was used in 500 μL PBST, and was washed with 40 mL PBST for 1.5 d (three times in total) for each antibody. We used stochastic electrotransport[28] to stain a 2-mm-thick slice with Alexa Fluor 647-conjugated rabbit anti-GFP antibody (Life Technologies, A31852) and Alexa Fluor 647-conjugated donkey anti-rabbit IgG antibody (Abcam, ab181347). For each antibody, we first electrotransported stochastically a solution containing 20 μL of antibody in 4 mL of 0.6 M N-cyclohexyl-3-aminopropanesulfonic acid (CAPS), 0.2 M Tris, 100 mM NaCl, 20 mM SDS, 1% BSA with an electrophoresis buffer containing 0.3 M CAPS, 0.2 M Tris, 20 mM SDS, 30% sorbitol for 21 h. It was then electrotransported stochastically in a solution containing 4 mL of 0.3 M CAPS, 0.2 M Tris, 20 mM SDS, 30% sorbitol, 1% BSA, and 1% Triton X-100 with an electrophoresis buffer containing 0.04 M Tris, 0.01 M phosphate, 30% sorbitol for 8 h. These two steps complete the stochastic electrotransport labeling. The stained sample was expanded in a solution containing 0.01% (wt/vol) heparin sodium porcine mucosa (Sigma, SRE0027) and 1% Triton X-100 in DI water, and then imaged.

Cell distortion analysis. Before and after MAP processing tubulin images were first registered using a scaled-rotation transformation in Fiji. Non-rigid invertible B-spline registration was performed with an 8 × 8 control point grid in bUnwarpJ. Vectors of different length were subjected to the resulting nonlinear transformation, and the input-output difference norm was sorted based on the input vector length and then averaged by root-mean-square. For morphological image processing of nuclei, TOTO-1 images before and after MAP-processing were first registered using a scaled-rotation transformation in Fiji. The registered images were segmented by thresholding and converted to circular particles with equivalent average radii calculated from the "Analyze Particles" function in Fiji. Matched pairs of cells from the before and after images were randomly chosen, and the expansion ratio was calculated from the ratio of the connecting line segment lengths. The fraction in nuclei was obtained by summing the intensity profile along the connecting line segment and averaging the sums from the before and after binary masks.

Tissue distortion analysis. After anesthesia, mice were first washed transcardially with 2% AA in PBS followed by perfusion with 4% PFA and 30% AA in PBS. Thy1-eGFP-M mouse brains were harvested and incubated in 20 mL of the same fixative solution at 4 °C overnight and at 37 °C for 3 h. Brains were sectioned to 100-μm-thick coronal slices with a vibrating microtome. Slices were stained and imaged to obtain "before MAP" images, and then incubated in a solution containing 4% PFA, 30% AA, 0.1% BA, 10% SA, and 0.1% V-50 in PBS at RT for 8 h. Hydrogel-tissue hybridization was performed *in situ* by incubating the tissues with nitrogen gas at 45 °C for 2 h. Hydrogel-embedded tissues were incubated in denaturation solution at 37 °C for 1 h and 95 °C for 0.5–1 h. Samples were then stained with the same markers and imaged to obtain "after MAP" images.

To quantify distortion errors, regions of ~3 mm × 2.5 mm in size that included cortex and hippocampus were stained with DyLight 594-conjugated lectin (Vector Laboratories, DL-1177) before (8 μL in 200 μL PBST for up to 8 samples) and after (2 μL in 200 μL PBST for each sample) MAP processing. Samples were incubated in RI matching solution after staining and mounted and imaged before MAP processing. Five samples were repeated for incubation, mounting and imaging to measure mounting errors. After MAP processing, six samples were stained, expanded in DI water, and imaged.

Keypoints of the vasculature in volumetric images were detected and matched between two image sets with a MATLAB code implementing the 3D Harris Corner Detector and 3D SIFT algorithm as described previously[13]. Using custom-built graphical user interface software developed with Delphi XE4 (Embarcadero Technologies), redundant keypoints closely located to each other and keypoints at tissue margins were removed. Tissue sizes were estimated by the area defined by a convex hull encompassing all keypoints, and the expansion ratio was calculated as the ratio between two squared roots of the areas. The correspondence information was used to generate a regularly spaced deformation mesh using a 3D thin plate spline code written by Yang (http://www.mathworks.com/matlabcentral/fileexchange/37576-3d-thin-plate-spline-warping-function). Lengths between each pair of grid points were calculated in both pre-MAP and post-MAP images, considering the expansion ratio. The difference between the two lengths was measured as a distortion error. After averaging the squared errors for each measurement length, the square root of the averages was collected from the samples to obtain statistical values of error.

Neurofilament tracing. Tracing of individual neurons was performed using either Fiji or Imaris. For manual tracing of a long tyrosine hydroxylase fiber, a representative fiber was chosen during confocal imaging acquisition and traced by moving the motorized stage and adjusting the z-level. During the tracing, ambiguous crossovers were resolved by obtaining high-magnification subvolume images. After tile-scanning, the target fiber was re-identified from the image volume using Fiji and marked to be displayed in a two-dimensional plane. For the semi-automatic tracing of SMI-312 fibers in a dense region, the entire 800 μm × 800 μm × 150 μm (expanded) data set was loaded along with a filament tool into a 'Surpass' instance using Imaris. An autopath calculation was performed using a single starting point as indicated in **Supplementary Video 8**. The fiber endpoint was designated by selecting the portion of the fiber exiting the imaged volume. The fiber representation was changed to a cone representation to visualize the filament diameter as well as the tracing path. The tracing fidelity was confirmed by inspection. To trace multiple fibers in a dense region, the full data set was cropped to the region indicated in **Figure 5o** using the '3D crop' tool, and similar autopath calculations were performed for each fiber. For traceability comparison between before and after MAP, we imaged the same tissues before and after MAP processing at the same resolution near the optical sampling limit with the Leica system and a 25×, 0.95 NA water-immersion objective. Two individuals not involved in imaging acquisition performed manual tracing using autodepth assistance in Imaris, and discordance ratios between manual tracing results before and after MAP processing were calculated.

Synaptic and fiber intensity profiles. The regions of interest were imported into Fiji. Lines were drawn perpendicular to the synaptic junction or near the fibers of interest and intensity profiles were obtained with adjusting the line width. For synaptic intensity profiles, two Gaussian distributions were fit to the distinct peaks by simultaneous minimization of the sum of squared residuals. Synaptic densities for bassoon and VGluT2 were calculated from three non-overlapping xy-images (235 μm × 235 μm) of expanded samples. The images were segmented by thresholding, and individual synaptic structures for each channel were counted using the "Analyze Particles" function in Fiji. The synaptic densities were calculated based on the frame area, and the s.d. was calculated from the three replicates.

34. Schindelin, J. *et al.* Fiji: an open-source platform for biological-image analysis. *Nat. Methods* **9**, 676–682 (2012).
35. Lancaster, M.A. & Knoblich, J.A. Generation of cerebral organoids from human pluripotent stem cells. *Nat. Protoc.* **9**, 2329–2340 (2014).